Roll Moment Characteristics of Supersonic Flight Vehicle Equipped with Asymmetric Protuberance

By Toshiaki HARADA,[1] Keiichi KITAMURA,[1] and Satoshi NONAKA[2]

[1]Department of System Integration, Yokohama National University, Yokohama, Japan
[2]Institute of Space and Astronautical Science, JAXA, Sagamihara, Japan

Most of flight vehicles have various protuberant devices on their surfaces, but asymmetry in their positioning with respect to the body axis can affect aerodynamic characteristics of vehicles, particularly roll moment. Thus, it is important in rocket development to clarify the effects of the protuberances on the vehicle aerodynamic characteristics. In this study, as a basic research, we systematically investigated such effects using CFD, by changing the positions of a protuberance. As a result, the roll moment increased nearly linearly with angle of attack (=α), but its trend was different in protuberance locations, particularly when arranged near the center-of-gravity. In positioning there at $\alpha = 20\,°$, the wake vortex center moved farther away from protuberance compared with $\alpha = 15\,°$, then the pressure decline at its wake side was suppressed, and thus, the pressure difference between its upstream and downstream sides became smaller. As a consequence, the roll moment did not arise linearly, but decreased at $\alpha = 20\,°$.

Key Words: Aerodynamics, Rockets, Computational Fluid Dynamics, Protuberance

Nomenclature

C_A	:	axial force coefficient, $-F_x/(q_\infty S_{ref})$
C_l	:	roll moment coefficient, $M_x/(q_\infty S_{ref}D)$
C_N	:	normal force coefficient, $-F_z/(q_\infty S_{ref})$
D	:	diameter of the vehicle
F_x	:	radius
F_z	:	length
h	:	height
L	:	total length of the vehicle
l	:	length
M	:	Mach number
M_x	:	roll moment
P	:	pressure
q	:	dynamic pressure
Re	:	Reynolds number
r	:	radius
S_{ref}	:	reference area, $\pi D^2/4$
T	:	temperature
u	:	x component of velocity
w	:	z component of velocity roll angle
α	:	angle of attack
φ	:	roll angle

Subscripts

0	:	stagnation point condition
∞	:	uniform condition
body	:	aerodynamic (body-fixed) coordinates
cg	:	center of gravity
L	:	total length of the vehicle
p	:	protuberance

1. Introduction

In recent years, a space development has been gaining popularity because of entries of private enterprises to space industry. Then, the demands of highly reliable space transportations are increasing.[1] In order to meet the demands, various studies[2-4] of rocket development such as aerodynamics are carried out. In the field of aerodynamics, researchers investigate aerodynamic characteristics of flight vehicles including rockets, and guarantee their flight feasibility.

Most of flight vehicles have various protuberant devices on their surfaces. Asymmetry in their positioning with respect to the vehicle body axis can affect aerodynamic characteristics of the vehicles, particularly roll moment.[5] In transonic and supersonic flows, shock waves are generated in front of protuberances, which more likely cause flow separations.[6] Such flow physics involving shocks and separated boundary-layers are complicated and their impact on the vehicle aerodynamics is therefore non-linear (unpredictable from a simple estimation based on existing data). Even though the heights of those protuberances are small compared with the radius of the vehicles, the aerodynamic forces created by them are known to make the vehicle roll.[5] Hence, for design and development of flight vehicles, it is important to clarify and examine the effect of the protuberances on the flow fields and the aerodynamic characteristics in detail.

In spite of the circumstances above, for any flight vehicles to date, acceptable protuberance locations and sizes have not been researched systematically yet. For example, the aerodynamic characteristics of Epsilon rocket[7] and M-V rocket[5] with protuberant devices were investigated in

references, but with their positions and sizes already determined.[4, 8] In this study, on the other hand, we clarify the effect of changing the protuberance positions on flow fields and the roll moment of a supersonic flight vehicle using CFD. The present results will provide us with the in-depth insight concerning the protuberance-equipped vehicle aerodynamics from academic point of view, but also will serve as a fundamental yet useful guideline in future vehicle designs.

2. Numerical Setup

2.1. Configuration for analysis

The configuration for this analysis is a simple rocket which is composed of an axisymmetric body (hemispherical cone + cylinder) and a nozzle parts. The hemispherical cone is defined as a fairing, and the connecting part between the fairing and cylinder is called as Fairing Shoulder. This configuration is named "Baseline" which is symmetric with respect to the body axis (Fig. 1(a)). The body length is L, the diameter is D, and the fineness ratio L / D is about 8.8. The base area of the cylinder is defined as the reference area S_{ref}. In addition, the center of gravity x_{cg} is about 56% of L. Now, the coordinate system (x, y, z) is defined as in Fig. 1(a) and this origin is corresponding the tip of the body. The x-axis is along the body axis of the vehicle, the y-axis is around which the angle-of-attack is defined, and the z axis is orthogonal those two, respectively.

The protuberance is modeled as shown in Fig. 1(b): This configuration is a hemisphere-cylinder, whose nearly half being immersed within the vehicle. This setup mimics an attitude control device[7] installed on typical rockets. The height h_p and the radius r_p of the protuberance are both $0.05D$, and the length l_p is $0.05L$. As shown in Fig. 1(c), we vary the positions of the protuberance as follows; i) Front; $x_p/L = 0.18$, ii) Middle; $x_p/L = 0.56$, and iii) Aft; $x_p/L = 0.98$. These positions are seen in general rockets. For example, Epsilon rocket has control devices and Falcon 9[9] has landing legs on aft of the body. Below a faring and around the center of gravity, cable ducts and pipe lines are seen in the other rockets. [4, 8] This is why we chose the three protuberance positions as in Fig. 1(c). Moreover, the position of the Middle is corresponding to x_{cg}. The roll angle of the protuberance is fixed at $\varphi = 90$ ° (in Fig. 1(d)) so that the protuberance-installed vehicle is asymmetric with respect to the freestream.

2.2 Computational method

In this study, we conduct three-dimensional numerical computation by using FaSTAR[10] developed at JAXA as the compressible flow solver for unstructured grids. The governing equations are the three-dimensional compressible Navier-Stokes equations discretized by cell-centered finite volume method. We use SLAU[11] to calculate a numerical flux of an inviscid term, Green-Gauss method[12] for a gradient reconstruction, and minmod[13] as a slope limiter. In addition, SA-noft2[14] is adapted as a turbulent model, and LU-SGS method[15] is selected as a time integration method. This calculation assumed a steady flow condition and converged because the fluctuation value of the roll moment is within 0.1% of the initial one. These computational methods are almost corresponding to Ref. 3).

2.3. Computational conditions

In this analysis, the freestream Mach number M_∞ is 1.5 and the Reynolds number Re_L is 1.2×10^7. We select these conditions by referring to the wind-tunnel test conditions in Ref. 2) in order to perform a validation of our computations in Sec. 3.2. The corresponding wind-tunnel conditions are shown in Table. 1. Then, α increases from 0 ° to 20 ° with 5 ° intervals. The definition of α will be mentioned in Sec. 2.5.

Table 1. Wind-tunnel test conditions.

M_∞ [-]	1.5
Re_L [-]	1.2×10^7
P_0 [kPa]	204
T_0 [K]	298

2.4. Computational grids

In this research, HexaGrid[16] developed at JAXA is used as the grid generation tool. It automatically generates unstructured grids based on hexahedral grids. The computational grid of Baseline case is shown in Fig. 2(a), as the representative example. As shown in Fig. 2(b), the outer boundary length is set as $10L$. Moreover, the number of cells for Baseline case is approximately 33 million. On the other hand, the number of cells for the other three cases (with a protuberance) is about 37 million because of the increased grid density around the protuberance. The first cell height (from the wall) is defined to satisfy $y^+ < 1$ in order to predict the boundary layer.

2.5. Aerodynamic coordinate system

As shown in Fig. 3, we define the aerodynamic coordinate system $(x_{body}, y_{body}, z_{body})$, which is different from the coordinate system (x, y, z) that mentioned in Fig. 1(a), but more useful to express the directions of aerodynamic forces. The center of this system is corresponding to the center of gravity x_{cg}. Moreover, the roll moment is defined around x_{body} axis (the positive roll moment is in counterclockwise direction when seen from the upstream).

3. Verification and Validation

3.1. Grid convergence (verification)

To verify the computational grid density, we checked the grid convergence by using C_A of Baseline case at $\alpha = 0$ °. As shown in Table. 2, C_A converges at the Medium grid, therefore, we adopted the Medium grid in the present analysis.
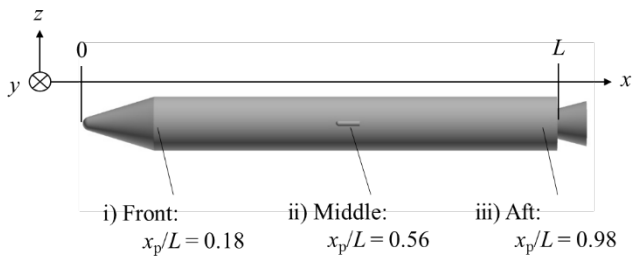
Table 2. Grid convergence.

Type of grid	Number of cells [$\times 10^6$]	C_A [-]
Coarse	2.8	0.598
Medium	3.3	0.599
Fine	4.2	0.599
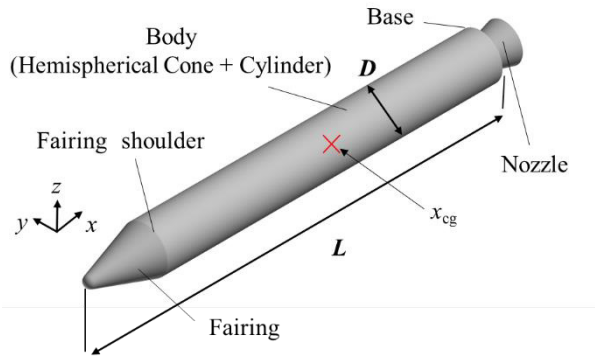
(a)   Baseline (body + nozzle).
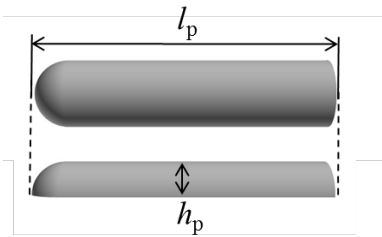
(b)   Protuberance (hemisphere-cylinder).

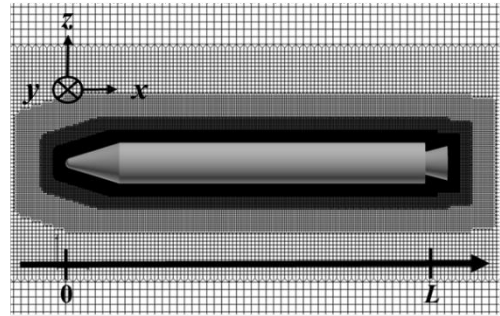i) Front: ii) Middle: iii) Aft:
$x_p/L = 0.18$ $x_p/L = 0.56$ $x_p/L = 0.98$
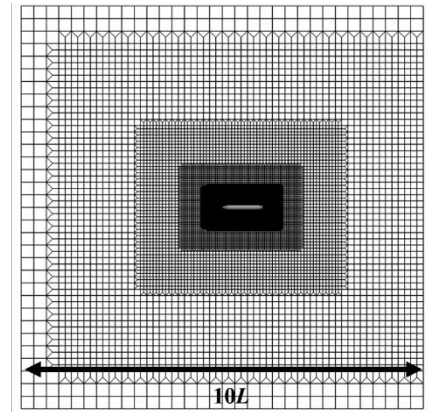
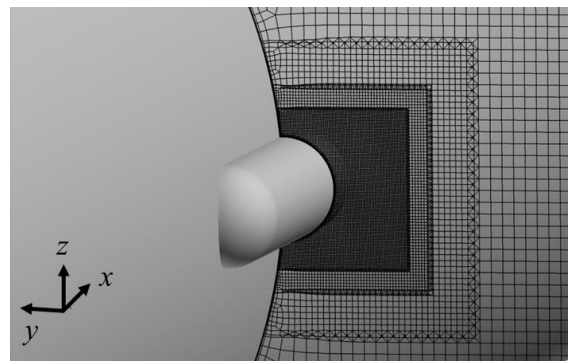(c)   Protuberance position (x axis).
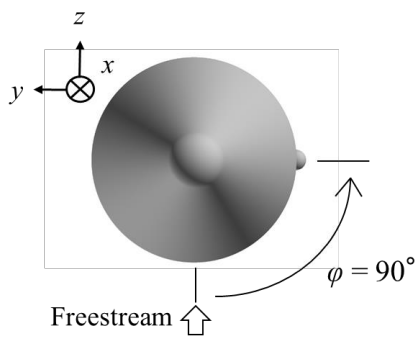
(d)   Protuberance position (roll angle).
Fig. 1.   Configuration for analysis.

(a)   Close-up view: body vicinity.

(b)   Overview.

(c)   Close-up view: protuberance.
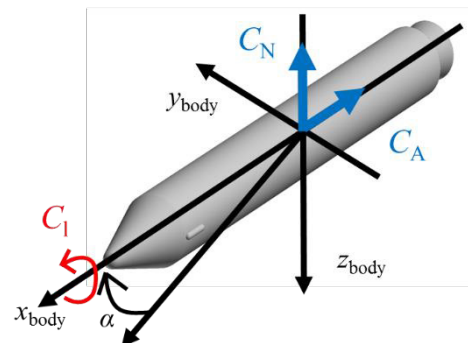Fig. 2.   Computational grid.

Fig. 3.   Aerodynamic coordinate system (x_{body}, y_{body}, z_{body}).

3.2. Comparison to experimental results (validation)

We validate the calculation result of Baseline case (without the protuberance) by comparison with the wind-tunnel test of Epsilon rocket obtained in JAXA,[2] because of the similar configuration adopted there.

As shown in Fig. 4, C_N of this study is compared to that of the Epsilon wind-tunnel tests from $\alpha = 0\,°$ to $10\,°$. As seen, until $\alpha = 6\,°$, C_N of both studies agree well with each other, which validates our computation. This non-linearity is associated with flow separations from the vehicle body and protuberances at higher angles-of-attack, and this explains the maximum discrepancy (nearly 9%) of C_N at $\alpha = 10\,°$. The C_N increases almost linearly for $\alpha < 6\,°$, but non-linearity gradually appears beyond that angle (Note that the Epsilon has many protuberances compared with the present vehicle configuration).

As for C_A, there is about 30% difference from the Epsilon wind-tunnel tests without protuberances and angle of attacks (Table 3). The cause of this difference is considered as the influence of sting and some gaps of the body shapes. In addition, by this calculation methods, we did not arrest the flow fields of the neighborhood of body base part, and this contributed to the disagreement of C_A. For these reasons, C_A did not accord, but we can say that the order of the calculations is right according to this comparison.
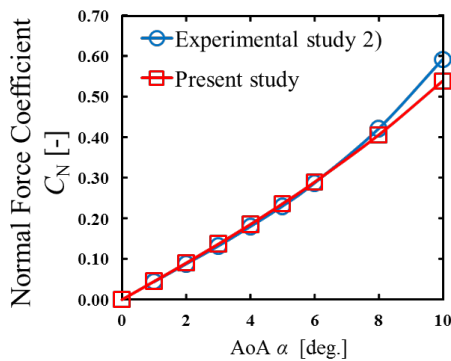

Fig. 4. α vs C_N in case without protuberance.

Table 3.   Comparison of C_A [-].

This result	0.599
Epsilon wind-tunnel test result	0.463

4.   Basic Flow Fields

In this chapter, the basic flow fields around the vehicle with the protuberance are described. The viewpoints in each figure of visualized results are shown in Fig. 5. In most of figures, visualized results of the $y = 0$ plane viewed from the $-y$ direction are displayed, as indicated in Fig. 5b. As for Fig. 6, however, visualized results of the $z = 0$ plane viewed from the $+z$ direction are shown (Fig. 5(a)).

The flow fields of the Middle case at $\alpha = 0\,°$ is mentioned as a representative case in Fig. 6. This figure shows the Mach number distribution on $z = 0$ plane, in which, several shock waves and expansion waves occur. The shock waves are formed in front of the rocket (SW1) and the protuberance (SW2), whereas the expansion waves (EW1 - EW5) arise from the fairing shoulder (EW1), the protuberance shoulder (EW2), the edge of the protuberance rear part (EW3), the edge of the body base (EW4) and the nozzle rear part (EW5). The Mach number is locally smaller behind shock waves, where the color of Mach number distribution is green in Fig. 6. On the other hand, the Mach number is locally larger behind the expansion waves, where the color of Mach number distribution is red. In turn, by visualizing the on-surface streamlines and the surface pressure distribution (Figs.7 and 8), we can confirm that the high pressure region occurs behind a shock wave, and after that the flow sprits into both outsides of the protuberance, associated with boundary layer separations. This flow structure is the same as that of the previous study (Ref. 3)). Moreover, we can find the horseshoe vortex[17] (Fig. 8) as reported in Ref. 3).

As for the base flow, a complicated, unsteady, and asymmetry flow fields are expected to be formed. However, since the unsteadiness of the complicated base flow phenomena is beyond the scope of our current work, we do not conduct unsteady flow simulations, but refer them to the future work.

(a) Fig. 6
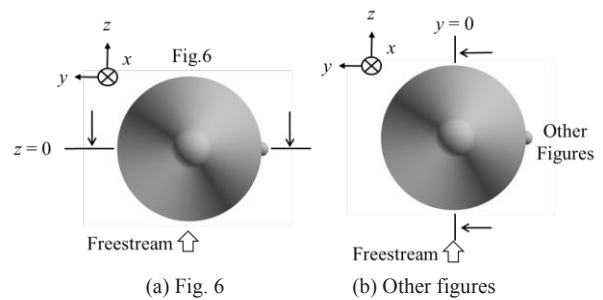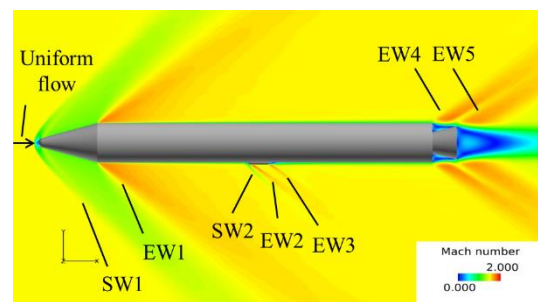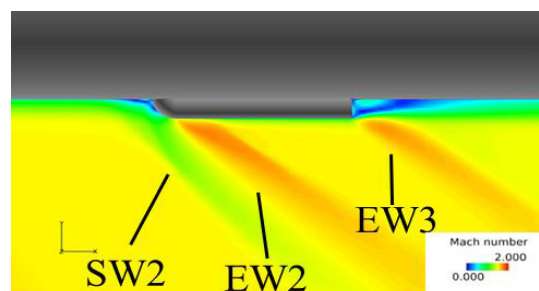(b) Other figures

Fig. 5.   Schematics of viewpoints.

(a)   Surroundings of vehicle.

(b)   Surroundings of protuberance.

Fig. 6.   Mach number distribution in Middle (plane at $z = 0$, viewed from $+z$).
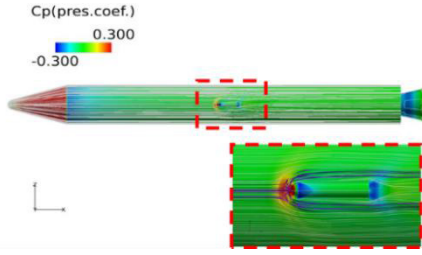
Fig. 7. Surface flow and pressure coefficient distribution in Middle (viewed from –y).
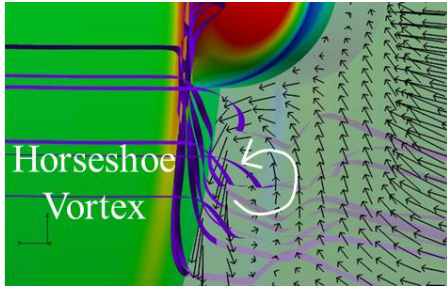

Fig. 8. Velocity vector around protuberance in Middle (the y-z plane, $x/L = 0.54$).
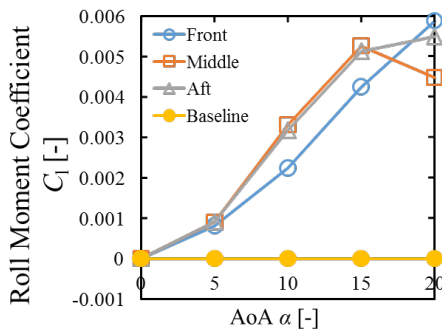

Fig. 9. α vs C_l.

Fig. 10. Mechanism of roll moment.

Fig. 11 Streamline around the protuberance and surface pressure distribution ($\alpha = 20$ °, the viewpoint from –y, (a)Front, (b)Middle, (c)Aft).

5. Results of Aerodynamic Coefficients

5.1. Generation of roll moment C_l

We have investigated the effects of protuberance positions on aerodynamic characteristics of the vehicle, such as roll moment, yaw moment, and side force. Since a remarkable trend has been found for the roll moment C_l, we will focus only on C_l in this paper.

We show the relation between C_l and α in Fig. 9. According to this graph, the roll moment is not produced in the Baseline case (without protuberance), of course. On the contrary, the roll moment is generated in the other cases (with protuberance). In addition, the trends of the roll moment depend on the protuberance position.

At first, let us explain the mechanism of the positive roll moment, which is around x_b-axis in the cases with the protuberance (Fig. 10). As shown in Fig. 10, the normal force is generated on the protuberance which is asymmetric with respect to the body axis: this force resulted in the roll moment.
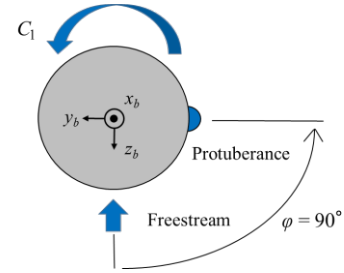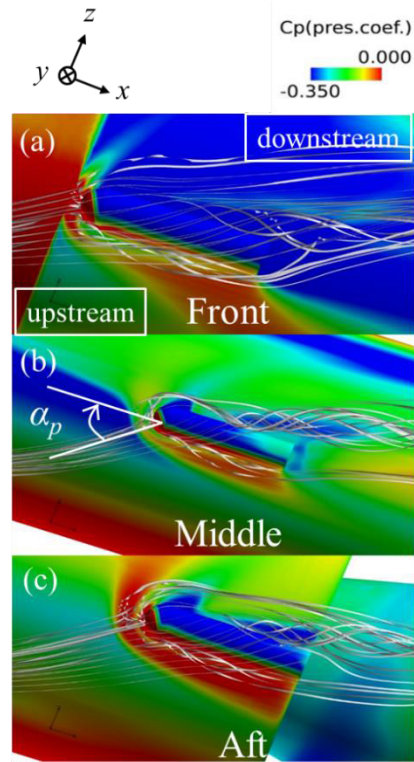
We will further investigate this from visualized results. The streamlines which hit against the protuberance in each case are shown in Fig. 11. Every streamline passes through the shock wave in front of the protuberance, runs into the protuberance, and creates a separation vortex in the downstream. Furthermore, according to the surface pressure distribution in Fig. 11, the pressure on the upstream side of the protuberance is locally high. This local high pressure has contributed to the positive roll moment.

5.2. Effects of protuberance position ($\alpha = 0$ ° - 15 °)

We consider the difference of the roll moment trends by the protuberant position. As shown in Fig. 9, the trend of Middle case resembles that of Aft case from $\alpha = 0$ ° to 15 °. As for Front case, the increasing tendency is also observed, but the slope is smaller; particularly at $\alpha = 10$ °, the roll moment is about 30% smaller than the others. Therefore, we explore the cause of these different tendencies due to protuberant positions.

At first, we focus on the upstream of the streamlines which will arrive at the protuberance. This set of streamlines firstly

impinge on the vehicle body after the uniform flow state, run along the side of the body, and then reach the protuberance. We visualize these streamlines at $\alpha = 15$ ° in Fig. 12. When the vehicle has angle of attacks, the vehicle parts (Fairing, Cylinder) along which the flow runs vary due to the protuberant positions (the positions where the flow impinges on the body are surrounded by red circles in this figure). In Front case, the flow streams along the fairing; on the other hand, in Middle and Aft cases, it runs along the cylinder of the body. This difference of the part which the flow impinges on and run along categorizes the tendencies of the roll moment from $\alpha = 0$ ° to 15 ° into two patterns; Front case and the others.

5.3. Decrease of roll moment ($\alpha = 15$ ° - 20 °)

Until $\alpha = 15$ °, the roll moment increases in all case, however, at $\alpha = 20$ °, the increasing trend of Middle case varies to the decreasing one, and the roll moment ($C_l = 0.0045$) is 23.9% smaller than that of Front case ($C_l = 0.0059$) and 18.5% smaller than that in the Aft case ($C_l = 0.0055$). Therefore, we investigate the roll moment decline from $\alpha = 15$ ° to $\alpha = 20$ ° in the Middle case and the reason why the roll moment takes the smaller value compared to the other cases at $\alpha = 20$ °. According to the visualized results in Fig. 13, we found that in the Middle case the surface pressure in the aft of the protuberance at $\alpha = 20$ ° is higher than $\alpha = 15$ °. Then the difference between the surface pressure of upstream and downstream sides is smaller at $\alpha = 20$ °, and the roll moment has declined eventually in the Middle case. In following, we investigate the reason why the downstream surface pressure increases from $\alpha = 15$ ° to $\alpha = 20$ ° in the Middle case.

We focus on the flow around the protuberance and introduce a new angle called "effective protuberance angle α_p", which is a local angle between the streamline hitting against the protuberance and the protuberance axis (Fig. 11). This angle is calculated from Eq. (1).

$$\alpha_p = \arctan\left(\frac{w}{u}\right) \quad [°] \qquad (1)$$

where u and w are the x and z components of the velocity vectors, respectively. In Eq. (1), we arbitrarily chose three streamlines (which later ran around the stagnation point), just before the shock waves in front of the protuberances; and then calculated each α_p; finally, these three α_p are averaged. Table 4 shows the calculated values.

Table 4. Effective protuberance angle α_p.

α [°]	Front	Middle	Aft
15	28	36	29
20	33	41	37

According to Table 4, the flow paths along which the flow runs appear to depend on the protuberant positions and α_p. In every case, α_p increases from $\alpha = 15$ ° to $\alpha = 20$ °. In addition, α_p takes the largest value in Middle case. So far, we have focused on the upstream side of the protuberance, but in the following we will also discuss the wake of the protuberance and its effect on the protuberance surface pressure. Figure 14 displays the velocity vectors on the y-z plane in the backward of the protuberance; 0.9 l_p plane at $\alpha = 20$ ° in order to visualize well-developed wake

near the protuberance (the plane position and view direction are indicated by the black arrows in Fig. 13). In this figure, the vortices are seen downstream the protuberance (the right side of the figure is the upstream, and the left side is the downstream). In every case, the separation (S1) occurs at the upper surface of the protuberance, and then a large separation vortex (V1) is generated (Fig. 14(a), (b), and (c)). In addition, two secondary vortices (V2, V3) are formed between the separation lines (S1, S2) in Fig. 14(d) and (e).

However, these secondary vortices are very small and these vortex structures are not found in the Middle case (Fig. 14(b)). Thus, V1 seems to dominate the downstream flow fields, and thus we will focus on V1. In the Front case, since the center of V1 is located near the protuberance, the pressure drop on the protuberance surface is observed (remembering the fact that the vortex center generally shows low pressure). However, in the Middle and Aft cases, this drop does not occur and the pressure in the backward of the protuberance is higher than that of Front case, as confirmed from the pressure-colored protuberance surface. Now, we will consider the relation between the pressure on the surface and d_v, which is the shortest distance from the center of V1 to the protuberance on the 0.9 l_p plane. Table 5 shows the non-dimensional values of d_v/h_p.

Table 5. Vortex center distance d_v/h_p.

α [°]	Front	Middle	Aft
15	0.45	0.90	0.65
20	0.55	1.73	0.95

According to Table 5, d_v/h_p increases from $\alpha = 15$ ° to $\alpha = 20$ ° in every case, but particularly, in Middle case, d_v/h_p significantly grows from 0.90 ($\alpha = 15$ °) to 1.73 ($\alpha = 20$ °). Using Tables 4 and 5, we drew the graph of α_p and d_v/h_p versus x_p/L as shown in Fig. 15. From this figure, α_p and d_v/h_p in the Middle case are the largest, these in the Front case are the smallest, and these in the Aft case are between the other two case. Moreover, in the Middle case, the effective protuberance angle α_p increases from 36 ° to 41 °, and then, d_v/h_p grows from 0.90 to 1.73, in which the center of V1 is farther from the protuberance than that of the other cases. Therefore, the surface pressure drop (which contributes to roll moment growth) at the backward of the protuberance drop hardly occurs at $\alpha = 20$ °, due to little influence from V1. As a result, the roll moment C_l decreased from 0.005 to 0.0045 (Fig. 9).

Similarly, in the Aft case, α_p becomes larger as seen in Fig. 15, however d_v/h_p does not increase so much compared to one in the Middle case. Glancing back at Fig.12, an angle at which the flow enters the shock wave in front of the vehicle was different between the cases of the Middle and Aft. Since in the Middle case the flow passes the shock wave at a larger angle (closer to right angle), a total pressure loss is larger there, and hence, the downstream flow has less momentum energy. Therefore, the flow separation can occur easily, and this is why the vortex easily moves farther away from the protuberance in Middle case. As a result, the increase rate of d_v/h_p is 92% in the Middle case, whereas it is 46% in the Aft case in which the center of V1 was closer to the protuberance.
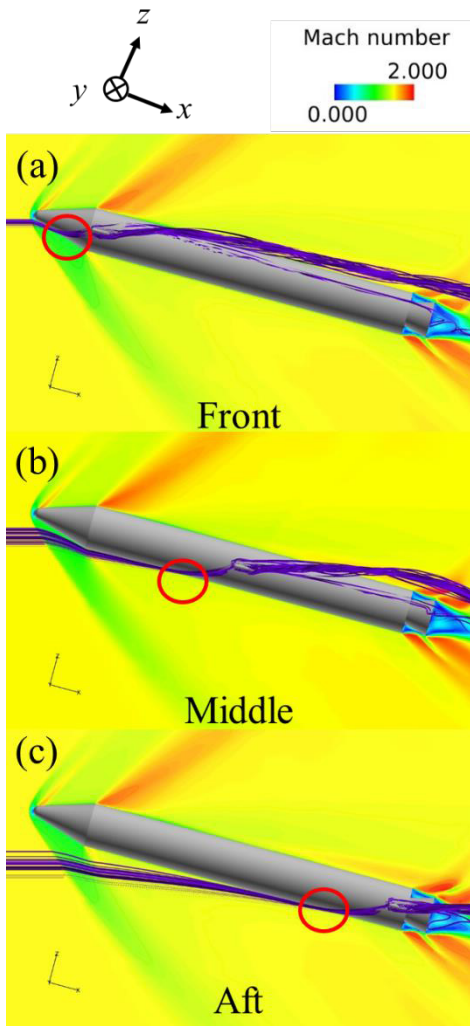
Fig. 12. Streamline which hit against the protuberance and Mach number distribution at $y = 0$ plane ($\alpha = 15\,°$, the viewpoint from $-y$, (a)Front, (b)Middle, (c)Aft).
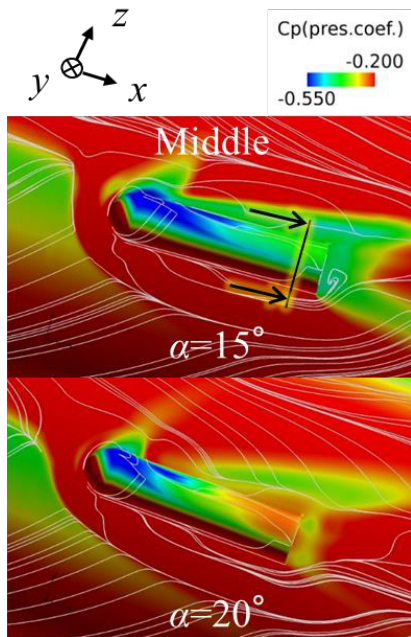

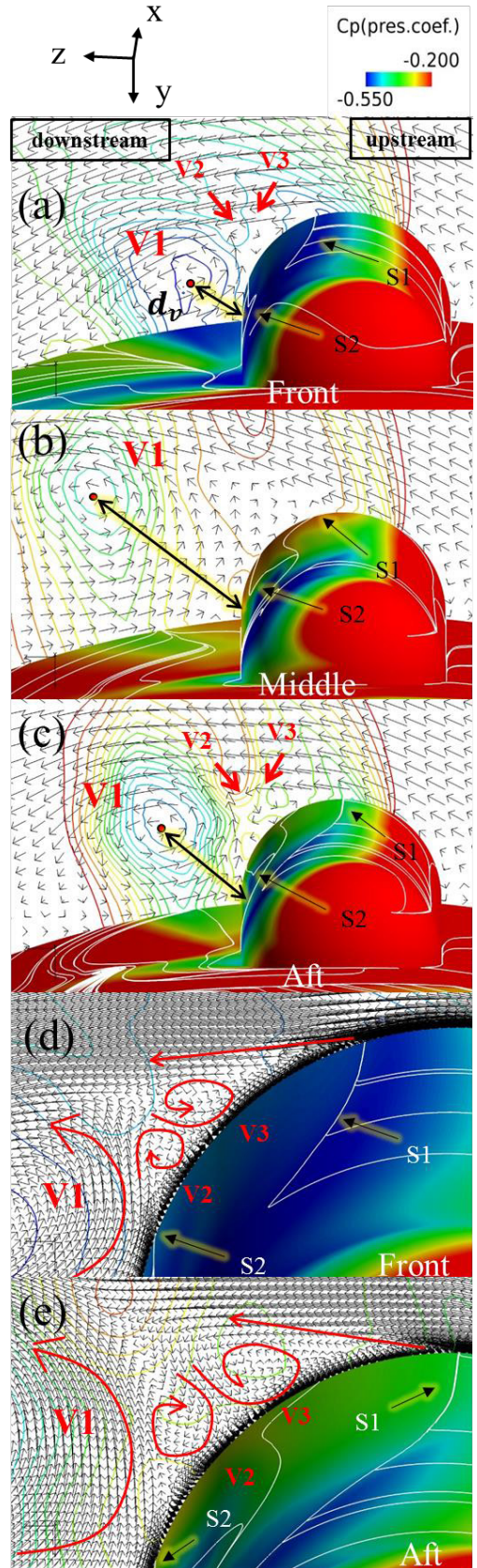Fig. 13. Comparative of surface pressure distribution (Middle).

Fig. 14. Velocity vector at the backward ($0.9l_p$) of the protuberance (at $\alpha = 20\,°$, (a)Front, (b)Middle, (c)Aft, (d)Front details, (e)Aft details).
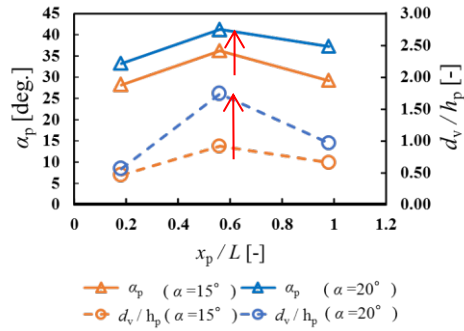
Fig. 15. α_p and d_v/h_p vs x_p/L (Front; x_p/L =0.18, Middle; x_p/L =0.56, Aft; x_p/L =0.98).

6. Conclusions

In this study, we clarified the effect of protuberance positions on the roll moment and the flow fields around the vehicle as a basic research using CFD. The positions of the protuberance are varied as follows; i) Front; x_p/L = 0.18, ii) Middle; x_p/L = 0.56, iii) Aft; x_p/L = 0.98. As for the roll angle of the protuberance, it is fixed at φ = 90 °. The summary of this paper is expanded below.

1. A separation shock wave occurs in the upstream of the protuberance, and then a high pressure region is generated on the upstream side of the protuberance surface. This region creates an asymmetric surface pressure distribution on the protuberance. This asymmetry appear as the normal force because the protuberance is located asymmetrically with respect to body axis. Therefore, this force leads to the roll moment of the vehicle.

2. We found different trends of the roll moment in each protuberant position as follows.
   a. $\alpha \leq$ 15 ° in the Front case, the flow firstly streams along the fairing and runs into the protuberance. On the other hand, in the Middle and Aft cases, the flows run along the cylinder part of the body. Therefore, the increasing trend of the roll moment are different between in the Front case and the other cases. In the Front case, the roll moment is smaller; particularly, at α = 10 °, it (C_l = 0.0022) is approximately 30% smaller than in the cases of other positions.
   b. The roll moment increases almost linearly for $\alpha \leq$ 15 ° in all case, however, nonlinearity appears at α = 20 °. In particular, the increasing trend of Middle case turns to the decreasing one. In order to investigate this roll moment decline, we defined an "effective protuberance angle α_p", which is the newly-introduced local angle between the streamline impinging on the protuberance and the body axis. In Middle case, α_p increases from 36 ° (α = 15 °) to 41 ° (α = 20 °). In addition, the larger the α_p is, the farther the center of the vortex, which dominates the flow fields of the protuberance wake, moves away from the protuberance. Therefore, the pressure drop by the vortex decreases in the

backward of the protuberance at α = 20 °. As a result, the difference between the pressure in the upstream side and the downstream side of the protuberance declines, and the roll moment is diminished from 0.0053 (α = 15 °) to 0.0045 (α = 20 °); specifically, this is 23.9% smaller than that in the Front case and 18.5% smaller than that in the Aft case.

References

1) Nakasuka, S., Kaneoka, M., Nakamura, Y., Inoue, K., Sugita, S., and Akiyama, H.: Panel Discussion "New Space Development and Utilization Opened by Micro-Satellites" Part I, *Aeronautical and Space Sciences Japan*, **64** (2014), pp.284-292 (in Japanese).

2) Kitamura, K., Fujimoto, K., Nonaka, S., Irikado, T., Fukuzoe, M., and Shima, E.: Wind Tunnel Tests on Aerodynamic Characteristics of Advanced Solid Rocket, *Trans. JSASS. Aerospace Technology. Japan*, **9** (2010), pp.9-14 (in Japanese).

3) Kitamura, K., Fujimoto, K., Kuzuo, K., Nonaka, S., Irikado, T., Fukuzoe, M., and Shima, E.: Numerical Analysis on Aerodynamic Characteristics of Advanced Solid Rocket, *Trans. JSASS. Aerospace Technology. Japan*, **10** (2011), pp.1-10 (in Japanese).

4) Panda, J., Martin, F. W., and Sutliff, D. L.: Estimation of the Unsteady Aerodynamics Load on Space Shuttle External Tank Protuberances from a Component Wind Tunnel Test, AIAA Paper 2008-0232, 2008.

5) Iizuka, N., Fujii, K., Fujimatsu, N., and Moriya, K.: CFD Analysis of the Rolling Moment Characteristics of M-V-5 Rocket, ISTS 2004-e-11, 24th International Symposium on Space Technology and Science, Miyazaki, Japan, Jun. 2004.

6) Aso, S., Maekawa, S., Karashima, K., and Sato, K.: The Experimental Studies on the Shock Wave/Turbulent Boundary Layer Interaction Region Induced by the Blunt Protuberance, *JSASS J.*, **44** (1996), pp. 735-740 (in Japanese).

7) Kitamura, K. Nonaka, S., Kuzuu, K., Aono, J., Fujimoto, K., and Shima, E.: Numerical and Experimental Investigations of Epsilon Launch Vehicle Aerodynamics at Mach 1.5, *J. Spacecraft and Rockets*, **50** (2013), pp. 896-916.

8) Hall, R. M. and Bauer, S. X.: Aerodynamic Characterization of the Ares Launch Vehicles, *J. Spacecraft and Rockets*, **49** (2012), pp. 558-563.

9) SpaceX, http://www.spacex.com/falcon9/ (accessed June 20, 2017).

10) Hashimoto, A., Murakami, K., Aoyama, T., Hishida, M., Ohno, S., Sakashita, M., Lahur, P., and Sato, Y.: Development of Fast Flow Solver FaSTAR, *Trans. Jpn. Soc. Aeronaut. Space Sci.*, **42** (2010), pp. 79-84 (in Japanese).

11) Yoon, S. and Jameson, A.: Lower-Upper Symmetric-Gauss-Seidel Method for the Euler and Navier-Stokes Equations, *AIAA J.*, **26** (1988), pp.1025-1026.

12) Marvriplis, D. J.: Revisiting the Least-Squares Procedure for Gradient Reconstruction on Unstructured, AIAA Paper 2003-3986, 2003.

13) Roe, P. L.: Characteristics-Based Schemes for the Euler Equations, *Ann. Rev. Fluid Mech.*, **18** (1986), pp.337-365

14) Spalart, P. and Allmaras, S.: A One-Equation Turbulence Model for Aerodynamic Flows, AIAA Paper 1992-439, 1992.

15) Kitamura, K., Shima, E., Fujimoto, K., and Wang, Z. J.: Performance of Low-Dissipation Euler Fluxes and Preconditioned LU-SGS at Low Speeds, *Commun. Compu. Phys.*, **10** (2011),

pp.90-119.

16) Hashimoto, A., Murakami, K., Aoyama, T., Yamamoto, M., Murayama, M., and Lahur, P. R.: Drag Prediction on NASA CRM Using Automatic Hexahedra Grid Generation Method, *J. Aircraft*, **51** (2014), pp.1172-1182.

17) Hunt, J. C. R., Abell, C. J., Peterka, J. A. and Woo, H.: Kinematical Studies of the Flows around Free or Surface-mounted Obstacles; Applying Topology to Flow Visualization, *J. Fluid Mech.*, **86** (1978), pp.179-200.